

## Chapter 2

# Model Description

---

### 2.1 Introduction

A two-dimensional (2D) vertically integrated model using a finite difference scheme was developed by Unnikrishnan et al. [1999] to simulate tides and tidal circulation on the shelf regions off the central west coast of India including the Gulf of Khambhat. We have used this 2D tidal model in the present study to simulate tides in the Bay of Bengal (as described in Chapter 4). After the validation of tidal model, we modified the model to simulate storm surges caused by cyclones (as described in Chapter 5).

The equation of continuity and momentum equations that describe the tide driven motion in shallow seas and the numerical techniques applied to solve these equations are presented in this chapter. The initial and boundary conditions are also discussed. In order to modify the tidal model to stimulate storm surges, the terms related to wind stress and the pressure field is included in the governing equations. This is described in Chapter 5.

### 2.2 Governing equations

The vertically integrated equation of continuity and momentum equations that govern the tidal model are as follows:

$$\frac{\partial \eta}{\partial t} + \frac{\partial U}{\partial x} + \frac{\partial V}{\partial y} = 0 \quad (2.1)$$

$$\frac{\partial U}{\partial t} + \frac{\partial}{\partial x}(uU) + \frac{\partial}{\partial y}(vU) - fV = -gH \frac{\partial \eta}{\partial x} - \frac{C_d U \sqrt{U^2 + V^2}}{H^2} + A_H \left( \frac{\partial^2 U}{\partial x^2} + \frac{\partial^2 U}{\partial y^2} \right) \quad (2.2)$$

$$\frac{\partial V}{\partial t} + \frac{\partial}{\partial x}(uV) + \frac{\partial}{\partial y}(vV) + fU = -gH \frac{\partial \eta}{\partial y} - \frac{C_d V \sqrt{U^2 + V^2}}{H^2} + A_H \left( \frac{\partial^2 V}{\partial x^2} + \frac{\partial^2 V}{\partial y^2} \right) \quad (2.3)$$

The symbols used in the above equations have the following meanings:

$t$	time (s), measured relative to the commencement of simulation,
$x, y$	rectangular Cartesian co-ordinates (m),
$\eta(x, y, t)$	free surface elevation (m) above Mean Sea Level (MSL),
$h(x, y)$	depth of sea bed below MSL (m),
$H(x, y, t)$	total depth of the sea bed (m), i.e. $H = h + \eta$ ,
$u(x, y, t)$	zonal component of vertically averaged velocity ( $ms^{-1}$ ) over a depth H,
$v(x, y, t)$	meridional component of the vertically averaged velocity ( $ms^{-1}$ ),
$U(x, y, t)$	x- directed vertically integrated transport ( $m^2s^{-1}$ ), $U = \int_{-h}^{\eta} u dz$ ,
$V(x, y, t)$	y - directed depth integrated transport ( $m^2s^{-1}$ ), $V = \int_{-h}^{\eta} v dz$ ,
$f$	Coriolis parameter ( $s^{-1}$ ), $f = 2\Omega \sin\phi$ ,
$\Omega$	Earth's angular velocity of rotation ( $s^{-1}$ ) $\Omega \approx 2\pi/(3600 \times 23.9333)$ ,
$\phi(x, y)$	latitude north ( $^\circ$ ) ( $\phi < 0$ in the Southern Hemisphere),
$\rho$	density of sea water, assumed constant at $\rho \approx 1027kgm^{-3}$ ,
$C_d$	coefficient of bottom friction,
$A_H$	coefficient of horizontal eddy viscosity ( $m^2s^{-1}$ ).

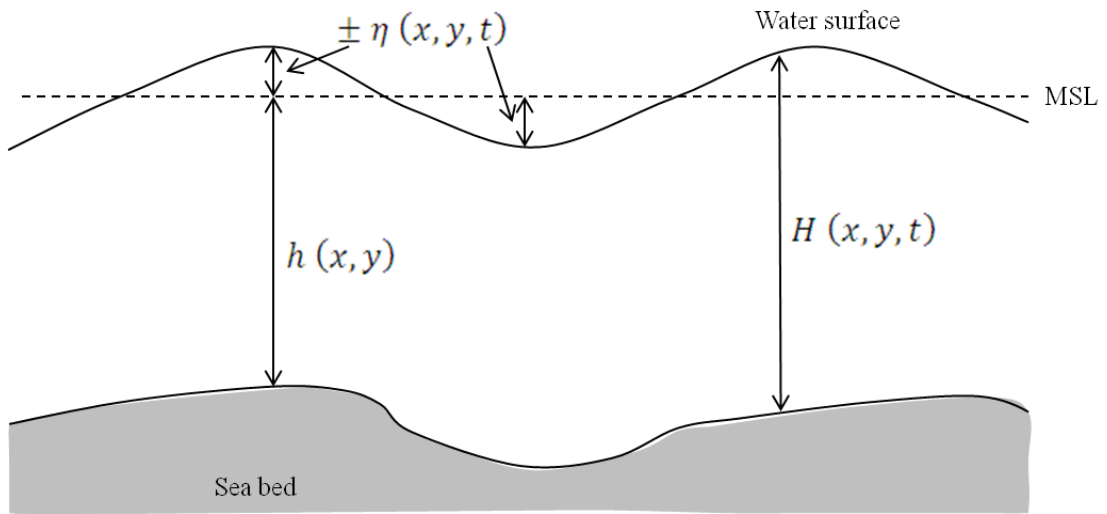
The variables  $\eta$ ,  $h$  and  $H$  are illustrated in Figure 2.1. The above equations in terms of vertically integrated transport have been employed in the tidal models developed by Sinha and Mitra [1988], Moe et al. [2002], Le Provost and Fornerino [1985].

### 2.3 Finite difference formulation

This section describes the numerical techniques used to solve Equations (2.1), (2.2) and (2.3). The first step towards numerical modelling is discretization, a process of converting the differential equations to a set of algebraic equations that can be computed using a computer. In the present study, we have used the method

of finite differences to discretize the above partial differential hydrodynamic equations.

**Figure 2.1** Schematic representation of  $\eta$ ,  $h$  and  $H$  for a water column in Cartesian coordinate system.



### 2.3.1 Finite differencing of spatial derivative

In the 2D model, the model domain is divided into uniform rectangular grids of fixed sizes in both  $x$  and  $y$  axes. The discretization procedure is elaborated as follows:

The horizontal  $x$  and  $y$  axes are divided into grids of uniform spacing  $\Delta x$  and  $\Delta y$  respectively, which results in a total of  $M \times N$  grid elements. The position of any grid element inside the model domain is represented as  $(x_i, y_j)$ , where

$$x_i = i\Delta x \quad \text{for } 1 \leq i \leq M \quad (2.4)$$

$$y_j = j\Delta y \quad \text{for } 1 \leq j \leq N \quad (2.5)$$

The variables, namely  $\eta$ ,  $u$  and  $v$  in the depth integrated equations are spatially staggered on these grids such that the sea surface elevation  $\eta$  is defined at the centre of the grid element and the velocity components are defined on the

corresponding faces of the grid. This grid arrangement is known as Arakawa C grid, as shown in Figure 2.2. The vertically integrated transport variables  $U$  and  $V$  are defined at the respective positions of  $u$  and  $v$ . Among the various Arakawa grids B, D and E, Arakawa C is the most commonly used staggered grid. Mesinger and Arakawa [1976] assessed that Arakawa C grid provides a more accurate representation of differential operator than the non-staggered Arakawa A grid.

The partial difference equations defined in Section 2.2 are numerically solved by converting the equations into finite difference form for each discrete grid elements. In general, the spatial derivatives of free surface elevation  $\eta$  in the hydrodynamic equation at a grid  $(i,j)$  can be represented in finite difference form in the following three ways:

$$\frac{\partial \eta}{\partial x} \cong \frac{\eta_{i+1} - \eta_i}{\Delta x} \quad (2.6)$$

$$\frac{d\eta}{dx} \cong \frac{\eta_{i+1} - \eta_{i-1}}{2\Delta x} \quad (2.7)$$

$$\frac{d\eta}{dx} \cong \frac{\eta_i - \eta_{i-1}}{\Delta x} \quad (2.8)$$

The approximations shown in Equations (2.6), (2.7) and (2.8) are known as forward, central and backward difference scheme, respectively.

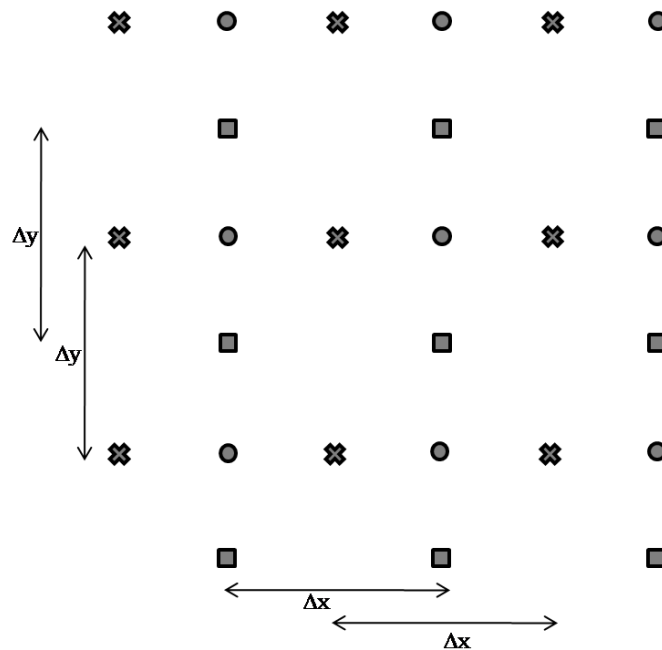
### **2.3.2 Finite differencing of time derivative**

The continuity Equation (2.1) consists of time derivative of the  $\eta$  and the momentum Equations (2.2) and (2.3) consists of time derivatives of  $U$  and  $V$ , respectively. The time derivative terms are approximated using a centered differencing scheme known as leap-frog method. This scheme also known as midpoint rule is defined by three time levels ( $k-1$ ,  $k$  and  $k+1$ ).

$$\frac{\partial \eta}{\partial t} = \frac{\eta_i^{k+1} - \eta_i^{k-1}}{2\Delta t} \quad (2.9)$$

Though leap-frog method is a neutrally stable efficient scheme with second order accuracy, the main drawback is generation of two solution - the real solution defined by the physical properties of the model and the unphysical solution known as computational mode produced due to the three time level numerical scheme. The computational mode is eliminated in the model by applying a two-level scheme at every 10 or 20 time step as the two level schemes do not generate computational mode [Kowalik and Murty, 1993].

**Figure 2.2** General layout of the Arakawa C grid showing the distribution of variables  $\eta$ ,  $u$  and  $v$  within a grid element with  $\bullet$  representing  $\eta$  point,  $\times$  representing the  $u$ ,  $U$  point and  $\blacksquare$  representing the  $v$ ,  $V$  point.



### 2.3.3 Relation between grid spacing and time step

The selection of grid spacing,  $\Delta x$  and  $\Delta y$ , depends on the size of the model domain and the resolution of the available bathymetric dataset. Though it is known that smaller grid sizes give more accurate results, the size of the grid spacing is limited by the time required for the simulation and availability of computational resources, such as computer memory capacity.

The temporal grid spacing,  $\Delta t$ , is determined based on the computational resources and the numerical stability criterion, which is related to the spatial grid spacing,  $\Delta x$  and  $\Delta y$ , selected for the model domain. The time step for the numerical model is selected so as to fulfil the Courant-Friedrichs-Levy (CFL) stability criteria, given as follows:

$$c \frac{\Delta t}{\sqrt{\Delta x^2 + \Delta y^2}} \leq 1 \quad (2.10)$$

which can be re-written using the expression for wave celerity  $c = \sqrt{gh}$  as

$$\Delta t \leq \frac{\sqrt{\Delta x^2 + \Delta y^2}}{\sqrt{gh}} \quad (2.11)$$

## 2.4 Finite difference form of governing equations

The numerical techniques described in Section 2.3 are employed in the tidal model to transfer the governing equations into finite difference form, which is described in the following section. The discretization of the terms constituting the Equations (2.1), (2.2) and (2.3) is different as the locations at which the discrete variables are specified differ within a grid element defined in the Cartesian coordinate system (North pointed upward along the y-axis).

- The variables  $\boldsymbol{\eta}_{i,j}$  and  $\boldsymbol{h}_{i,j}$  for grid  $(i,j)$  at a time level  $k$ , are specified at the centre of the grid  $(i,j)$  symbolically represented by position  $\left(i - \frac{1}{2}, j - \frac{1}{2}\right)$  and defined as  $\eta$  point

$$\boldsymbol{\eta}_{i,j}^k = \boldsymbol{\eta}_{i-\frac{1}{2},j-\frac{1}{2}}^k \quad (2.12)$$

$$\boldsymbol{h}_{i,j} = \boldsymbol{h}_{i-\frac{1}{2},j-\frac{1}{2}} \quad (2.13)$$

- The velocity component  $\mathbf{U}_{i,j}$  and  $\mathbf{u}_{i,j}$  for a  $(i,j)^{th}$  grid at a time level  $k$  are positioned to the east of  $\eta$  point at the midpoint of the side parallel to y-axis symbolically represented by position  $\left(i - \frac{1}{2}, j - \frac{1}{2}\right)$  and specified as  $U$  point

$$\mathbf{U}_{i,j}^k = U_{i,j-\frac{1}{2}}^k \quad (2.14)$$

- The velocity component  $\mathbf{V}_{i,j}$  and  $\mathbf{v}_{i,j}$ , for a  $(i,j)^{th}$  grid at a time level  $k$  are specified to the north of  $\eta$  point at the midpoint of the parallel to x-axis symbolically represented by position  $\left(i - \frac{1}{2}, j - \frac{1}{2}\right)$  and is called as  $V$  point.

$$\mathbf{V}_{i,j}^n = V_{i-\frac{1}{2},j}^k \quad (2.15)$$

where  $i = 2, M; j = 2, N; k = 1, K$

The discretization of the variables for the grid  $(i,j)$  and the surrounding grid is shown in Figure 2.3.

### 2.4.1 Treatment of continuity equation

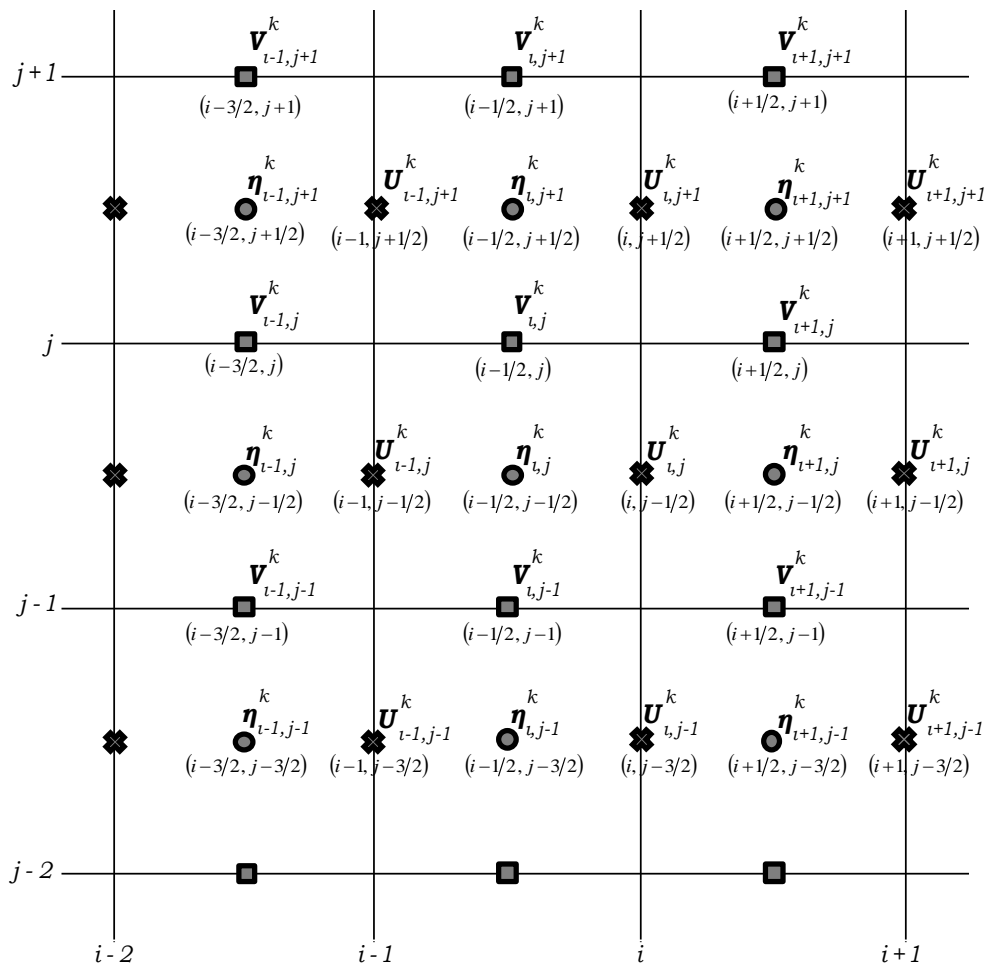
The derivatives in Equation (2.1) are approximated into finite difference formulae using leap-frog method to march in time and centred differencing about the location of  $\eta$  point for a  $(i,j)^{th}$  grid, which yield the following:

$$\left(\frac{\partial \eta}{\partial t}\right)_{i-\frac{1}{2},j-\frac{1}{2}}^k = \frac{\eta_{i-\frac{1}{2},j-\frac{1}{2}}^{k+1} - \eta_{i-\frac{1}{2},j-\frac{1}{2}}^{k-1}}{2\Delta t} = \frac{\boldsymbol{\eta}_{i,j}^{k+1} - \boldsymbol{\eta}_{i,j}^{k-1}}{2\Delta t} \quad (2.16)$$

$$\left(\frac{\partial U}{\partial x}\right)_{i-\frac{1}{2},j-\frac{1}{2}}^k = \left(\frac{U_{i,j-\frac{1}{2}}^k - U_{i-1,j-\frac{1}{2}}^k}{\Delta x}\right) = \left(\frac{\mathbf{U}_{i,j}^k - \mathbf{U}_{i-1,j}^k}{\Delta x}\right) \quad (2.17)$$

$$\left(\frac{\partial V}{\partial y}\right)_{i-\frac{1}{2},j-\frac{1}{2}}^k = \left(\frac{V_{i-\frac{1}{2},j}^k - V_{i-\frac{1}{2},j-1}^k}{\Delta y}\right) = \left(\frac{\mathbf{V}_{i,j}^k - \mathbf{V}_{i,j-1}^k}{\Delta y}\right) \quad (2.18)$$

**Figure 2.3** Definition of  $\eta$ ,  $U$  and  $V$  point staggered on the computational grid  $(i, j)$  and the grids surrounding it. The positions of these points in terms of  $i, j$  are indicated symbolically.





### 2.4.2 Treatment of advective term

The finite difference of the advective term in Equation (2.2) along x-direction is derived using centred differencing and averaging around the location of  $U$  point:

$$\begin{aligned}
\left(\frac{\partial(uU)}{\partial x}\right)_{i,j-\frac{1}{2}}^k &\approx \frac{1}{\Delta x} \left[ (uU)_{i+\frac{1}{2},j-\frac{1}{2}}^k - (uU)_{i-\frac{1}{2},j-\frac{1}{2}}^k \right] \\
&\approx \frac{1}{\Delta x} \left[ u_{i+\frac{1}{2},j-\frac{1}{2}}^k U_{i+\frac{1}{2},j-\frac{1}{2}}^k - u_{i-\frac{1}{2},j-\frac{1}{2}}^k U_{i-\frac{1}{2},j-\frac{1}{2}}^k \right] \\
&\approx \frac{1}{\Delta x} \left[ \left( \frac{u_{i+1,j-\frac{1}{2}}^k + u_{i,j-\frac{1}{2}}^k}{2} \right) \left( \frac{U_{i+1,j-\frac{1}{2}}^k + U_{i,j-\frac{1}{2}}^k}{2} \right) \right. \\
&\quad \left. - \left( \frac{u_{i,j-\frac{1}{2}}^k + u_{i-1,j-\frac{1}{2}}^k}{2} \right) \left( \frac{U_{i,j-\frac{1}{2}}^k + U_{i-1,j-\frac{1}{2}}^k}{2} \right) \right] \\
&= \frac{1}{\Delta x} \left[ \frac{1}{4} (\mathbf{u}_{i+1,j}^k + \mathbf{u}_{i,j}^k) (\mathbf{U}_{i+1,j}^k + \mathbf{U}_{i,j}^k) \right. \\
&\quad \left. - \frac{1}{4} (\mathbf{u}_{i,j}^k + \mathbf{u}_{i-1,j}^k) (\mathbf{U}_{i,j}^k + \mathbf{U}_{i-1,j}^k) \right] \quad (2.19)
\end{aligned}$$

$$\begin{aligned}
\left(\frac{\partial(vU)}{\partial y}\right)_{i,j-\frac{1}{2}}^k &\approx \frac{1}{\Delta y} [(vU)_{i,j}^k - (vU)_{i,j-1}^k] \\
&\approx \frac{1}{\Delta y} [v_{i,j}^k U_{i,j}^k - v_{i,j-1}^k U_{i,j-1}^k] \\
&\approx \frac{1}{\Delta y} \left[ \left( \frac{v_{i+\frac{1}{2},j}^k + v_{i-\frac{1}{2},j}^k}{2} \right) \left( \frac{U_{i,j+\frac{1}{2}}^k + U_{i,j-\frac{1}{2}}^k}{2} \right) \right. \\
&\quad \left. - \left( \frac{v_{i+\frac{1}{2},j-1}^k + v_{i-\frac{1}{2},j-1}^k}{2} \right) \left( \frac{U_{i,j-\frac{1}{2}}^k + U_{i,j-\frac{3}{2}}^k}{2} \right) \right] \\
&= \frac{1}{\Delta y} \left[ \frac{1}{4} (\mathbf{v}_{i+1,j}^k + \mathbf{v}_{i,j}^k) (\mathbf{U}_{i,j+1}^k + \mathbf{U}_{i,j}^k) \right. \\
&\quad \left. - \frac{1}{4} (\mathbf{v}_{i+1,j-1}^k + \mathbf{v}_{i,j-1}^k) (\mathbf{U}_{i,j}^k + \mathbf{U}_{i,j-1}^k) \right] \quad (2.20)
\end{aligned}$$

The finite difference of the advective term in y-directed momentum Equation (2.3) is derived following similar procedures using centred differencing and centred space averaging for the derivatives, but around the location of  $V$  point.

### 2.4.3 Treatment of Coriolis term

The coriolis term in Equations (2.2) and (2.3) requires evaluation of  $V$  (y-directed depth integrated transport) at a  $U$  point and evaluation of  $U$  (x-directed depth integrated transport) at a  $V$  point respectively. This is achieved through centered averaging of  $V$  defined at the four  $V$  points surrounding the  $U$  point for Equation (2.2);

$$\begin{aligned}
 fV_{ij-\frac{1}{2}}^k &\approx f \left( \frac{V_{i+\frac{1}{2}j-\frac{1}{2}}^k + V_{i-\frac{1}{2}j-\frac{1}{2}}^k}{2} \right) \\
 &\approx \frac{f}{2} \left( \frac{V_{i+\frac{1}{2}j}^k + V_{i+\frac{1}{2}j-1}^k}{2} + \frac{V_{i-\frac{1}{2}j}^k + V_{i-\frac{1}{2}j-1}^k}{2} \right) \\
 &\approx \frac{f}{4} (V_{i+1,j}^k + V_{i+1,j-1}^k + V_{i,j}^k + V_{i,j-1}^k) \quad (2.21)
 \end{aligned}$$

A similar approach is taken to define  $U$  at  $V$  point for Equation (2.3).

### 2.4.4 Treatment of pressure gradient term

The pressure gradient term in Equations (2.2) and (2.3) is represented with total depth and space derivative of  $\eta$ . In the adopted Arakawa C grid, the total depth  $H = (h + \eta)$ , a function of both space and time, is prescribed at the  $\eta$  point. Therefore, depth at  $U$  point at a time level  $k$  for Equation (2.2) is defined by centred averaging:

$$\begin{aligned}
 \left( gH \frac{\partial \eta}{\partial x} \right)_{ij-\frac{1}{2}}^k &\approx g \left( \frac{H_{i+\frac{1}{2}j-\frac{1}{2}}^k + H_{i-\frac{1}{2}j-\frac{1}{2}}^k}{2} \right) \left( \frac{\eta_{i+\frac{1}{2}j-\frac{1}{2}}^k - \eta_{i-\frac{1}{2}j-\frac{1}{2}}^k}{\Delta x} \right) \\
 &= g \left( \frac{H_{i+1,j}^k + H_{i,j}^k}{2} \right) \left( \frac{\eta_{i+1,j}^k - \eta_{i,j}^k}{\Delta x} \right) \\
 &= g \left( \frac{h_{i,j} + h_{i+1,j} + \eta_{i,j}^k + \eta_{i+1,j}^k}{2} \right) \left( \frac{\eta_{i+1,j}^k - \eta_{i,j}^k}{\Delta x} \right) \quad (2.22)
 \end{aligned}$$

### 2.4.5 Treatment of viscosity term

The eddy viscosity terms in Equations (2.2) and (2.3) involve second order derivatives, which can be approximated using centred differencing about the position.

$$\begin{aligned} \left(\frac{\partial^2 U}{\partial x^2}\right)_{i,j-\frac{1}{2}}^k &\approx \frac{U_{i+1,j-\frac{1}{2}}^k - 2U_{i,j-\frac{1}{2}}^k + U_{i-1,j-\frac{1}{2}}^k}{(\Delta x)^2} \\ &= \left(\frac{U_{i+1,j}^k - 2U_{i,j}^k + U_{i-1,j}^k}{(\Delta x)^2}\right) \end{aligned} \quad (2.23)$$

$$\begin{aligned} \left(\frac{\partial^2 U}{\partial y^2}\right)_{i,j-\frac{1}{2}}^k &\approx \frac{U_{i,j+\frac{1}{2}}^k - 2U_{i,j-\frac{1}{2}}^k + U_{i,j-\frac{3}{2}}^k}{(\Delta y)^2} \\ &= \frac{U_{i,j+1}^k - 2U_{i,j}^k + U_{i,j-1}^k}{(\Delta y)^2} \end{aligned} \quad (2.24)$$

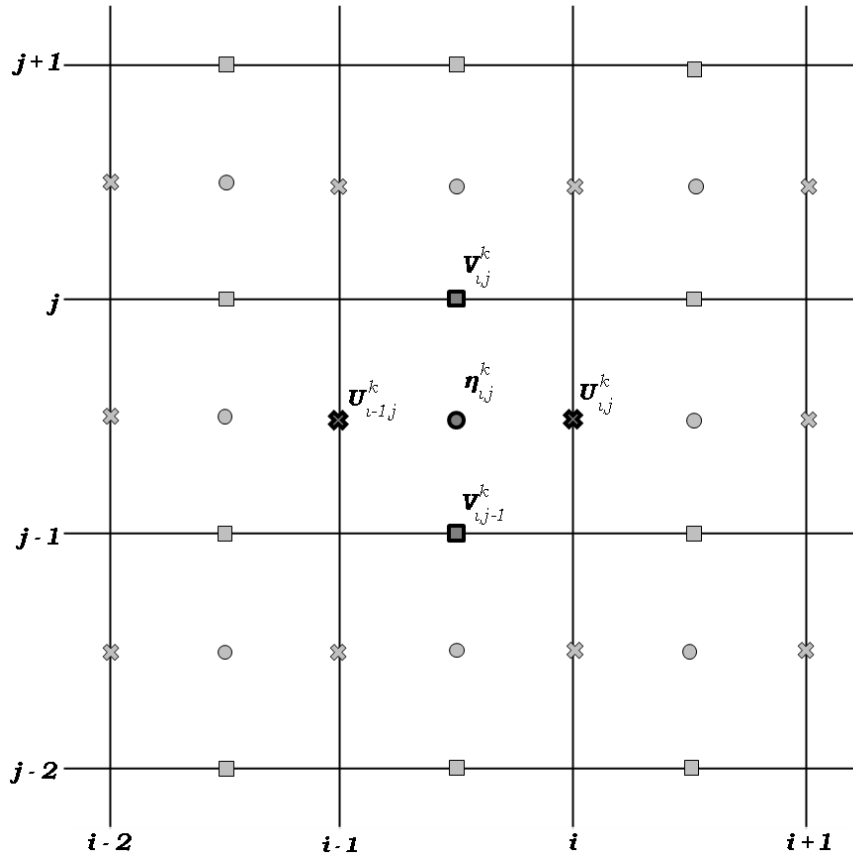
### 2.4.6 Continuity equation in finite difference form

The continuity equation in finite difference form is as follows

$$\boldsymbol{\eta}_{i,j}^{k+1} = \boldsymbol{\eta}_{i,j}^{k-1} - 2\Delta t \left( \frac{U_{i,j}^k - U_{i-1,j}^k}{\Delta x} + \frac{V_{i,j}^k - V_{i,j-1}^k}{\Delta y} \right) \quad (2.25)$$

Equation (2.25) represents the explicit numerical method as the equation at any spatial grid location includes only one unknown variable  $\boldsymbol{\eta}_{i,j}^{k+1}$ . The unknown variable  $\boldsymbol{\eta}_{i,j}$  at new time step  $(k+1)$  is computed from the 3 known value at previous time levels  $k$  and  $k-1$ . The variables used in Equation (2.25) to compute  $\boldsymbol{\eta}_{i,j}^{k+1}$  and their distribution on the Arakawa C grid with respect to grid  $(i,j)$  are shown in Figure 2.4.

**Figure 2.4** Schematic representation of the distribution of  $\eta$ ,  $U$  and  $V$  points that are used in Equation (2.1) to compute  $\eta_{i,j}^{k+1}$



### 2.4.7 Momentum equations in finite difference form

The finite difference form of Equations (2.2) and (2.3) time level  $k$ , therefore, can be defined by approximating the time derivative using leap-frog method and combining the difference terms derived in Equations (2.19) to (2.25), as shown in Equations (2.26) and (2.27). The distribution of variables used in these equations to compute  $U_{i,j}^{k+1}$  and  $V_{i,j}^{k+1}$  is shown in Figures 2.5 and 2.6, respectively. Since the leap-frog technique is employed to march forward in time, we have applied a two level scheme at every 20 time step to remove the computational mode as suggested by Kowalik and Murty [1993].

$$\begin{aligned}
\mathbf{U}_{i,j}^{k+1} = \mathbf{U}_{i,j}^{k-1} + 2\Delta t & \left[ -\frac{1}{4\Delta x} \{(\mathbf{u}_{i+1,j}^k + \mathbf{u}_{i,j}^k)(\mathbf{U}_{i+1,j}^k + \mathbf{U}_{i,j}^k) \right. \\
& - (\mathbf{u}_{i,j}^k + \mathbf{u}_{i-1,j}^k)(\mathbf{U}_{i,j}^k + \mathbf{U}_{i-1,j}^k)\} \\
& - \frac{1}{4\Delta y} \{(\mathbf{v}_{i+1,j}^k + \mathbf{v}_{i,j}^k)(\mathbf{U}_{i,j+1}^k + \mathbf{U}_{i,j}^k) - (\mathbf{v}_{i+1,j-1}^k + \mathbf{v}_{i,j-1}^k)(\mathbf{U}_{i,j}^k + \mathbf{U}_{i,j-1}^k)\} \\
& + \frac{f}{4} (\mathbf{v}_{i+1,j}^k + \mathbf{v}_{i+1,j-1}^k + \mathbf{v}_{i,j}^k + \mathbf{v}_{i,j-1}^k) \\
& - \frac{g}{2\Delta x} (\mathbf{h}_{i,j} + \mathbf{h}_{i+1,j} + \boldsymbol{\eta}_{i,j}^k + \boldsymbol{\eta}_{i+1,j}^k)(\boldsymbol{\eta}_{i+1,j}^k - \boldsymbol{\eta}_{i,j}^k) \\
& + A_H \left\{ \frac{1}{(\Delta x)^2} (\mathbf{U}_{i+1,j}^{k-1} - 2\mathbf{U}_{i,j}^{k-1} + \mathbf{U}_{i-1,j}^{k-1}) \right. \\
& + \left. \frac{1}{(\Delta y)^2} (\mathbf{U}_{i,j+1}^{k-1} - 2\mathbf{U}_{i,j}^{k-1} + \mathbf{U}_{i,j-1}^{k-1}) \right\} \\
& + \frac{C_d \mathbf{U}_{i,j}^{k-1} \sqrt{(\mathbf{U}_{i,j}^{k-1} \times \mathbf{U}_{i,j}^{k-1}) + (\mathbf{v}_{i,j}^{k-1} \times \mathbf{v}_{i,j}^{k-1})}}{(\mathbf{h}_{i,j} + \boldsymbol{\eta}_{i,j}^{k-1})^2} \Big]
\end{aligned} \tag{2.26}$$

$$\begin{aligned}
\mathbf{U}_{i,j}^{k+1} = \mathbf{U}_{i,j}^{k-1} + 2\Delta t & \left[ -\frac{1}{4\Delta x} \{(\mathbf{u}_{i+1,j}^k + \mathbf{u}_{i,j}^k)(\mathbf{U}_{i+1,j}^k + \mathbf{U}_{i,j}^k) \right. \\
& - (\mathbf{u}_{i,j}^k + \mathbf{u}_{i-1,j}^k)(\mathbf{U}_{i,j}^k + \mathbf{U}_{i-1,j}^k)\} \\
& - \frac{1}{4\Delta y} \{(\mathbf{v}_{i+1,j}^k + \mathbf{v}_{i,j}^k)(\mathbf{U}_{i,j+1}^k + \mathbf{U}_{i,j}^k) - (\mathbf{v}_{i+1,j-1}^k + \mathbf{v}_{i,j-1}^k)(\mathbf{U}_{i,j}^k + \mathbf{U}_{i,j-1}^k)\} \\
& + \frac{f}{4} (\mathbf{v}_{i+1,j}^k + \mathbf{v}_{i+1,j-1}^k + \mathbf{v}_{i,j}^k + \mathbf{v}_{i,j-1}^k) \\
& - \frac{g}{2\Delta x} (\mathbf{h}_{i,j} + \mathbf{h}_{i+1,j} + \boldsymbol{\eta}_{i,j}^k + \boldsymbol{\eta}_{i+1,j}^k)(\boldsymbol{\eta}_{i+1,j}^k - \boldsymbol{\eta}_{i,j}^k) \\
& + A_H \left\{ \frac{1}{(\Delta x)^2} (\mathbf{U}_{i+1,j}^{k-1} - 2\mathbf{U}_{i,j}^{k-1} + \mathbf{U}_{i-1,j}^{k-1}) \right. \\
& + \left. \frac{1}{(\Delta y)^2} (\mathbf{U}_{i,j+1}^{k-1} - 2\mathbf{U}_{i,j}^{k-1} + \mathbf{U}_{i,j-1}^{k-1}) \right\} \\
& + \frac{C_d \mathbf{U}_{i,j}^{k-1} \sqrt{(\mathbf{U}_{i,j}^{k-1} \times \mathbf{U}_{i,j}^{k-1}) + (\mathbf{v}_{i,j}^{k-1} \times \mathbf{v}_{i,j}^{k-1})}}{(\mathbf{h}_{i,j} + \boldsymbol{\eta}_{i,j}^{k-1})^2} \Big]
\end{aligned} \tag{2.27}$$

**Figure 2.5** Same as Figure 2.4, but showing the distribution of variable used in Equation (2.2) to compute  $U_{i,j}^{k+1}$ .

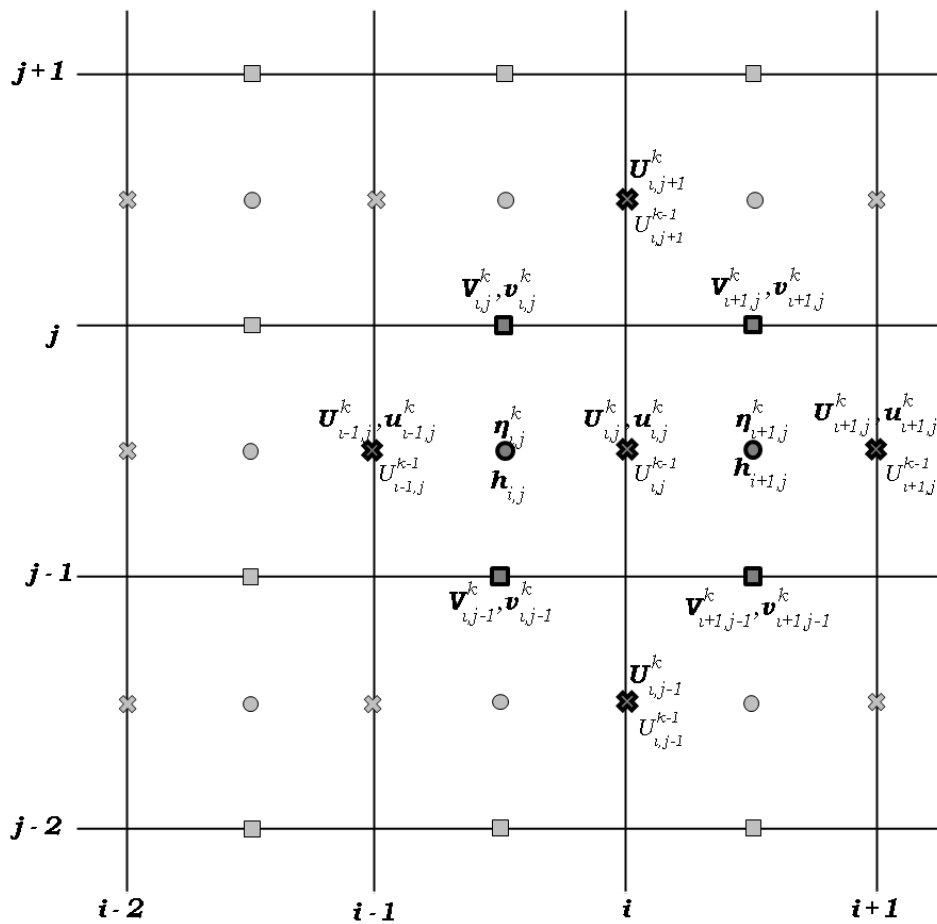
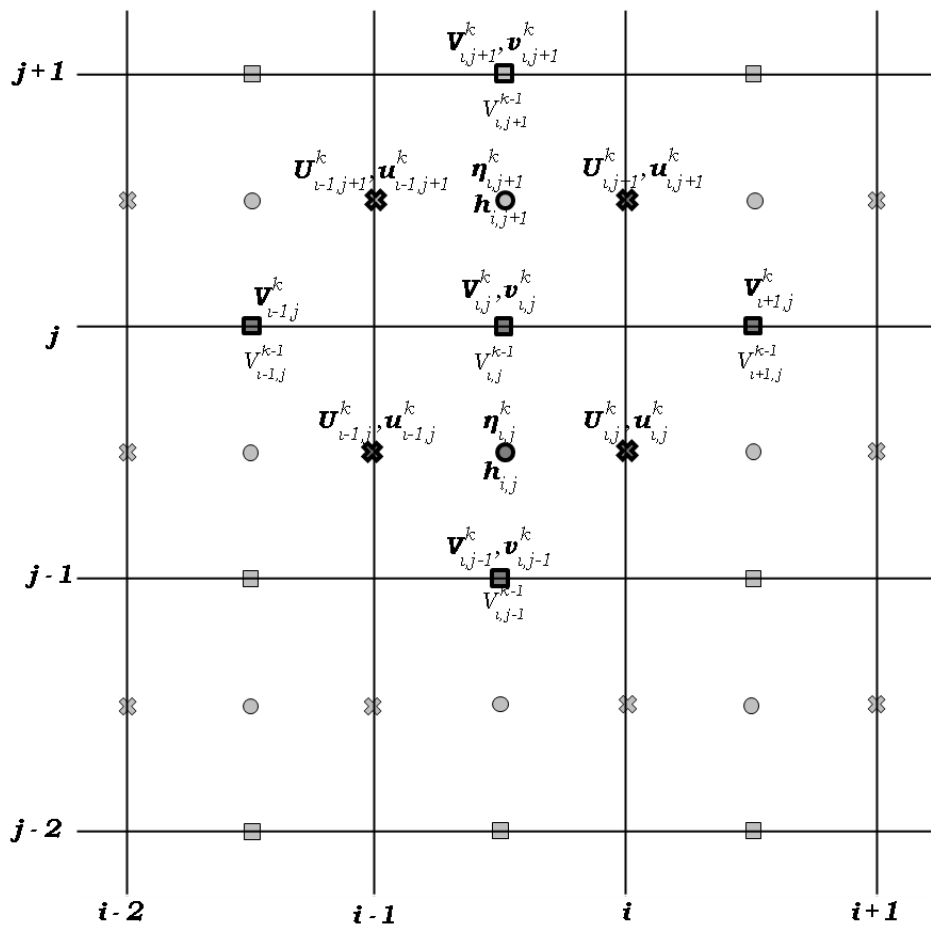


**Figure 2.6** Same as Figure 2.4, but showing the distribution of variable used in Equation (2.3) to compute  $V_{ij}^{k+1}$ .



## 2.5 The initial and boundary conditions

It is essential to define the appropriate initial and boundary conditions for numerical solution of the equations.

### 2.5.1 Initial conditions

The initial conditions to be specified in the numerical model are defined as follows:

$$\begin{aligned} \eta(x, y, 0) &= \eta_0(x, y), \\ U(x, y, 0) &= U_0(x, y), \\ \text{and} \quad V(x, y, 0) &= V_0(x, y) \end{aligned} \quad (2.28)$$

where  $\eta_0$ ,  $U_0$  and  $V_0$  are the elevation and velocity fields at time  $t = 0$ . Since the actual values for initial elevations and velocities are not available, a ‘cold start’ is specified, which is a standard practise:

$$\eta(x, y, 0) = U(x, y, 0) = V(x, y, 0) = 0 \quad (2.29)$$

In order to remove any instability produced by this approximation, the numerical model is run for sufficient spin-up period so that any initial disturbance caused by this condition is assumed to disappear within this period.

### 2.5.2 Closed boundary conditions

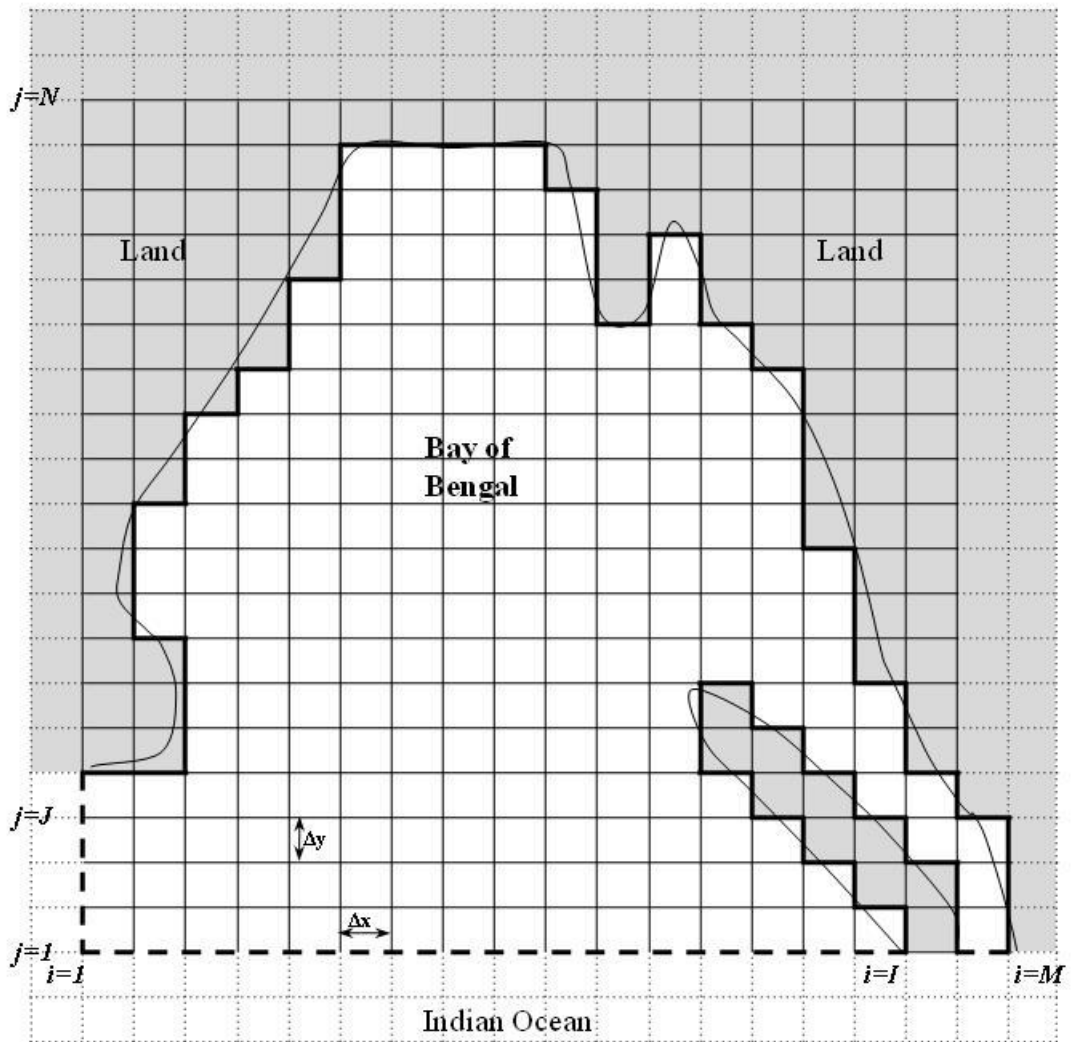
The boundary between land and sea represents the closed boundaries in the tidal model.

#### Coastal boundary

The boundary between land and sea in the domain, i.e the physical coastline is approximated as impermeable walls parallel to either x-axis or y-axis as shown in Figure 2.7 representing a solid boundary with no flow across it. The thin curved line in Figure 2.7 shows the schematic physical coastline and thick straight lines define the approximated coastal boundary of the model. Along the coastal boundaries, zero normal flux and slip conditions were applied.



**Figure 2.7** Schematic representation of actual coastal boundaries (thin solid line) into orthogonal vertical walls (thick solid line) representing the closed boundaries. The shaded area (grey) represents land and the dashed line represents the open boundaries. All boundaries are shown indicatively and out of scale for clarity.



### Surface boundary

The treatment of surface boundary plays an important role in storm surge model in which wind force is allowed to act on the sea surface and to move its surface tangentially through frictional forces. Since this chapter includes description of tidal model alone, the description of surface wind stresses  $\tau_{sx}$  and  $\tau_{sy}$ , that will be included in momentum Equations (2.2) and (2.3) for the storm surge model, is presented in Chapter 5. As represented by Equations (2.2) and (2.3) if there is only tidal forcing (no wind),

$$\tau_{sx} = \tau_{sy} = 0 \quad (2.30)$$

### Seabed

The sea bed is also a solid boundary which does not allow water to pass through. The closed boundary at seabed is also treated with a free slip condition, whereby the velocity at the sea bed is not set to zero but a value obtained from an appropriate quadratic friction law that relates frictional stress directly to the velocity at the bed. The bottom stress  $\tau_b$  is defined as:

$$\tau_b = \rho C_D |u|u \quad (2.31)$$

where  $C_D$  is coefficient of bottom friction which usually lies between  $1 \times 10^{-3}$  and  $3 \times 10^{-3}$ .

### 2.5.3 Open boundary conditions

Open boundaries are not real physical boundaries but represent the artificial edge of the model domain that meet the open ocean. The driving force of tidal as well as storm surge model is provided at the open boundary, mainly in the form of tidal elevation. Since the storm surge model includes additional driving force in the form of wind applied at the surface, the open boundary conditions formulated for the tidal model and storm surge model are different.

The model domain consists of three open boundaries – one is on the western side and two are on the southern side, which are schematically shown as dashed lines in Figure 2.7. A height specified boundary condition is applied to the

tidal model, in which the tidal elevation  $\eta_{i,j}$  is specified for all time at each  $\eta$  point of the grid element  $(i, j)$  along the open boundaries, where  $i = 1, I; j = 1$  for the southern boundaries and  $i = 1; j = 1, J$  for the western boundary. The values of  $I$  and  $J$  are selected such that the grid elements  $(I+1, 1)$  and  $(1, J+1)$  represent land. Since the open boundary connects the model domain to the open ocean, as shown in Figure 2.7, the tidal elevation at each grid element along the open boundary is obtained from Global Tidal Model. The tidal elevation ( $\eta_{i,j}$ ), is then used to compute the velocity components at each grid element along the boundary using Equations (2.2) and (2.3). However, due to lack of some computational values, the numerical formulation of these equations along the open boundaries is different from the Equations (2.26) and (2.27).

In order to compute the velocity components along the southern open boundary, the finite difference Equations (2.26) and (2.27) are simplified by neglecting the terms that include undefined variables like  $U_{i,j-1}$ . The equations formulated for the grid elements at the two ends of the southern boundaries -  $(1,1)$  and  $(I,1)$  and at any grid element  $(i,1)$  are different due to the difference in the arrangement of the surrounding grids. The simplified finite difference form of Equations (2.2) and (2.3) for the three scenarios are presented below:

**Grid element  $(I, 1)$**

$$\mathbf{U}_{i,j}^{k+1} = \mathbf{U}_{i,j}^{k-1} + 2\Delta t \left[ \begin{aligned} &+ \frac{f}{2} (\mathbf{v}_{i+1,j}^k + \mathbf{v}_{i,j}^k) \\ &- \frac{g}{2\Delta x} (\mathbf{h}_{i,j} + \mathbf{h}_{i+1,j} + \boldsymbol{\eta}_{i,j}^k + \boldsymbol{\eta}_{i+1,j}^k) (\boldsymbol{\eta}_{i+1,j}^k - \boldsymbol{\eta}_{i,j}^k) \\ &+ \frac{C_d \mathbf{U}_{i,j}^{k-1} \sqrt{(\mathbf{U}_{i,j}^{k-1} \times \mathbf{U}_{i,j}^{k-1}) + (\mathbf{v}_{i,j}^{k-1} \times \mathbf{v}_{i,j}^{k-1})}}{(\mathbf{h}_{i,j} + \boldsymbol{\eta}_{i,j}^{k-1})^2} \end{aligned} \right] \quad (2.32)$$

$$\begin{aligned}
\mathbf{v}_{i,j}^{k+1} = \mathbf{v}_{i,j}^{k-1} + 2\Delta t & \left[ \frac{f}{3} (\mathbf{u}_{i,j+1}^k + \mathbf{u}_{i-1,j+1}^k + \mathbf{u}_{i,j}^k) \right. \\
& - \frac{g}{2\Delta y} (\mathbf{h}_{i,j} + \mathbf{h}_{i,j+1} + \boldsymbol{\eta}_{i,j}^k + \boldsymbol{\eta}_{i,j+1}^k) (\boldsymbol{\eta}_{i,j+1}^k - \boldsymbol{\eta}_{i,j}^k) \\
& \left. + \frac{C_d \mathbf{v}_{i,j}^{k-1} \sqrt{(\mathbf{u}_{i,j}^{k-1} \times \mathbf{u}_{i,j}^{k-1}) + (\mathbf{v}_{i,j}^{k-1} \times \mathbf{v}_{i,j}^{k-1})}}{(\mathbf{h}_{i,j} + \boldsymbol{\eta}_{i,j}^{k-1})^2} \right] \quad (2.33)
\end{aligned}$$

**Grid element (I, 1)**

$$\mathbf{u}_{i,j}^{k+1} = 0.0 \quad (2.34)$$

$$\begin{aligned}
\mathbf{v}_{i,j}^{k+1} = \mathbf{v}_{i,j}^{k-1} + 2\Delta t & \left[ + \frac{f}{2} (\mathbf{u}_{i-1,j+1}^k + \mathbf{u}_{i-1,j}^k) \right. \\
& - \frac{g}{2\Delta y} (\mathbf{h}_{i,j} + \mathbf{h}_{i,j+1} + \boldsymbol{\eta}_{i,j}^k + \boldsymbol{\eta}_{i,j+1}^k) (\boldsymbol{\eta}_{i,j+1}^k - \boldsymbol{\eta}_{i,j}^k) \\
& \left. + \frac{C_d \mathbf{v}_{i,j}^{k-1} \sqrt{(\mathbf{u}_{i,j}^{k-1} \times \mathbf{u}_{i,j}^{k-1}) + (\mathbf{v}_{i,j}^{k-1} \times \mathbf{v}_{i,j}^{k-1})}}{(\mathbf{h}_{i,j} + \boldsymbol{\eta}_{i,j}^{k-1})^2} \right] \quad (2.35)
\end{aligned}$$

**Grid element (i, 1)**

$$\begin{aligned}
\mathbf{u}_{i,j}^{k+1} = \mathbf{u}_{i,j}^{k-1} + 2\Delta t & \left[ \frac{f}{2} (\mathbf{v}_{i+1,j}^k + \mathbf{v}_{i,j}^k) - \frac{g}{2\Delta x} (\mathbf{h}_{i,j} + \mathbf{h}_{i+1,j} + \boldsymbol{\eta}_{i,j}^k + \boldsymbol{\eta}_{i+1,j}^k) (\boldsymbol{\eta}_{i+1,j}^k - \boldsymbol{\eta}_{i,j}^k) \right. \\
& + A_H \left\{ \frac{1}{(\Delta x)^2} (\mathbf{u}_{i+1,j}^{k-1} - 2\mathbf{u}_{i,j}^{k-1} + \mathbf{u}_{i-1,j}^{k-1}) \right. \\
& \left. + \frac{1}{(\Delta y)^2} (\mathbf{u}_{i,j+2}^{k-1} - 2\mathbf{u}_{i,j+1}^{k-1} + \mathbf{u}_{i,j}^{k-1}) \right\} \\
& \left. + \frac{C_d \mathbf{u}_{i,j}^{k-1} \sqrt{(\mathbf{u}_{i,j}^{k-1} \times \mathbf{u}_{i,j}^{k-1}) + (\mathbf{v}_{i,j}^{k-1} \times \mathbf{v}_{i,j}^{k-1})}}{(\mathbf{h}_{i,j} + \boldsymbol{\eta}_{i,j}^{k-1})^2} \right] \quad (2.36)
\end{aligned}$$

$$\begin{aligned}
\mathbf{V}_{i,j}^{k+1} = \mathbf{V}_{i,j}^{k-1} + 2\Delta t & \left[ \frac{f}{4} (\mathbf{U}_{i,j+1}^k + \mathbf{U}_{i-1,j+1}^k + \mathbf{U}_{i,j}^k + \mathbf{U}_{i-1,j}^k) \right. \\
& - \frac{g}{2\Delta y} (\mathbf{h}_{i,j} + \mathbf{h}_{i,j+1} + \boldsymbol{\eta}_{i,j}^k + \boldsymbol{\eta}_{i,j+1}^k) (\boldsymbol{\eta}_{i,j+1}^k - \boldsymbol{\eta}_{i,j}^k) \\
& + A_H \left\{ \frac{1}{(\Delta x)^2} (\mathbf{V}_{i+1,j}^{k-1} - 2\mathbf{V}_{i,j}^{k-1} + \mathbf{V}_{i-1,j}^{k-1}) + \frac{1}{(\Delta y)^2} (\mathbf{V}_{i,j+2}^{k-1} - 2\mathbf{V}_{i,j+1}^{k-1} + \mathbf{V}_{i,j}^{k-1}) \right\} \\
& \left. + \frac{C_d \mathbf{V}_{i,j}^{k-1} \sqrt{(\mathbf{U}_{i,j}^{k-1} \times \mathbf{U}_{i,j}^{k-1}) + (\mathbf{V}_{i,j}^{k-1} \times \mathbf{V}_{i,j}^{k-1})}}{(\mathbf{h}_{i,j} + \boldsymbol{\eta}_{i,j}^{k-1})^2} \right]
\end{aligned} \tag{2.37}$$

Similar equations are derived and applied for the western open boundary by neglecting terms that include un-defined variables such as  $V_{i-1,j}$ .

In the tidal model, a height specified boundary condition can be used as there are no internal flows produced by any wind forcing. However, in the storm surge model, which is driven by a combination of two forces: wind force applied at the surface and tidal elevation specified at the open boundary, a radiation type boundary condition is applied at the open boundaries. This will allow outward passage of the any internal waves generated within the model domain by wind action. The radiation type boundary condition is presented in Chapter 5.

## 2.6 Summary

The numerical techniques used to solve the vertically integrated hydrodynamic equations that govern the tidal model, are illustrated. The spatial and temporal discretization of the governing equations to represent them in finite difference form is investigated in detail and summarized in the chapter. The understanding of these techniques and formulations is essential to comprehend the basics of the tide and storm surge model, the application of which will be described in the following chapters. The most significant input data required for the numerical model is bathymetry. The generation of an accurate bathymetric dataset for the Bay of Bengal region is discussed in next chapter.

## Chapter 3

# Generation of bathymetric datasets for numerical model

---

### 3.1 Introduction

It is well known that the performance of a numerical model depends on accurate representation of sea bed levels. A variety of bathymetric datasets with different coverage, resolutions, and accuracies are currently available. Among these is the ETOPO5 [National Geophysical Data Centre (NGDC), 1988] bathymetric grids which are widely used.

ETOPO5 is a 5-arc minute bathymetry grid produced by combining the ocean depth values obtained from DBDB-5 [US National Geospatial-Intelligence Agency, 1994] with the land elevation data obtained from different sources. The DBDB-5 (Digital Bathymetric Data Base 5) dataset was generated by digitizing the depth contours above 200 m from hydrographic charts of nominally 1:4,000,000 scale. The digitized values were gridded to a 5 arc minute grid using a multi-stage minimum-curvature spline interpolation algorithm. Digitization was carried out only for depths greater than 200 m as DBDB-5 was designed to be used only as a deep-water data base [Goodwillie, 2003]. Subsequently, the ETOPO5 dataset is not accurate in regions where the depth values are less than 200 m.

The region of interest, in the present study, is the Bay of Bengal. The head bay, the Gulf of Martaban and Malacca Strait which form parts of the present study region, are characterised by very shallow depths, wide continental shelf and sudden changes in depth contours. These characteristics are not represented in a global dataset such as ETOPO5. We noted that there are no open source accurate shallow water bathymetric dataset available for the Bay of Bengal. Therefore, we

decided to generate bathymetric dataset for the shallow regions of Bay of Bengal. However, while undertaking the task, we observed that the shallow-water usage of bathymetric datasets for the entire Indian Ocean are often not as coordinated internationally and not as standardized as deep-water datasets leading to the use of different sources of bathymetric data by different ocean modellers. For example, Unnikrishnan et al. [1999], for their tidal model, digitized the hydrographic charts of the region to get a more accurate bathymetry to obtain improved model results. In order to avoid such inconsistencies in model results due to the use of bathymetric data from different sources, a common dataset for shallow waters in the entire Indian Ocean is very essential. This need has become urgent after the disastrous tsunami of 26 December 2004 that occurred in the Indian Ocean. Tsunami simulations are critically dependent on the bathymetry used, as are the source-region estimates based on backward ray tracing [Lay et al., 2005a, b; Neetu et al., 2005].

The task to generate reliable bathymetry on the continental shelves of the Bay of Bengal was, therefore, extended to cover the shallow regions of the Indian Ocean north of 38°S. To achieve this, we digitized the hydrographic charts listed in Table 3.1 (published by the National Hydrographic Office (NHO), Dehradun, India - formerly known as the Naval Hydrographic Office till 1998) for depths less than 200 m. Since ETOPO5 dataset is reliable in deep waters, the newly generated shelf bathymetry was blended with the deep water ETOPO5 bathymetry to develop a full bathymetric dataset. The generation and reliability of the modified bathymetric datasets has been documented in detail in Sindhu et al. [2007].

The methodology adopted to generate the shallow water bathymetry is elaborated in Section 3.2 and the improvements of the modified datasets over the original ETOPO5 dataset is demonstrated in Section 3.3. The modified ETOPO5 is foreseen to serve the ocean modellers as common datasets for the shallow regions in the Indian Ocean.

**Table 3.1** List of hydrographic charts used for digitization, their natural scale, and year of publication for different regions in the Indian Ocean.

	<b>Charts</b>	<b>Scale</b>	<b>Year</b>
1	Walvis Bay to Lorencu Marques	1:3,500,000	1975
2	Lorencu Marques to Mogadiscio	1:3,500,000	1971
3	Indian Ocean: Western portion	1:10,000,000	1979
4	Gulf of Aden: Eastern portion including Socatra Island	1:750,000	1982
5	Gulf of Aden and Southern part of Red Sea	1:750,000	1978
6	Red Sea	1:2,250,000	1973
7	Arabian Sea	1:3,500,000	1974
8	Strait of Hormuz to Qatar	1:750,000	1982
9	Qatar to Shatt Al Arab	1:750,000	1982
10	Muscat to Mumbai (Bombay)	1:1,500,000	1980
11	Gwadar to Dwarka	1:750,000	1979
12	Mumbai (Bombay) to Cape Comorin	1:1,500,000	1980
13	Cochin to Vishakhapatnam	1:1,500,000	1974
14	Bay of Bengal: Northern Side (Krishnapatnam to Bassein river)	1:1,500,000	1976
15	Andaman Sea	1:1,500,000	1979
16	Maldivu Islands to Sumatra	1:3,500,000	1973
17	South China Sea	1:3,500,000	1976
18	Cora Divh to Elikalpeni bank	1:500,000	1983
19	Central Lakshwadeep	1:300,000	1983
20	Ihavandiffulu atoll to Horsburgh atoll	1:300,000	1981
21	Horsburgh atoll to Haddummati atoll	1:300,000	1982
22	Haddummati atoll to Addu atoll	1:300,000	1981
23	Chagos Archipelago	1:375,000	1984
24	Chagos Archipelago to Malagasy	1:3,500,000	1974



## 3.2 Data and methodology

### 3.2.1 Generation of improved bathymetric grids

The extent of each of the hydrographic charts, used for digitization is shown in Figure 3.1. The nautical charts and the allied nautical publications produced by NHO have built the reputation of the organisation all over the world for their accuracies [Ahuja, 2000]. The database used in the preparation of these charts have been obtained from different sources of information like hydrographic survey, local survey, ocean soundings, earlier editions of nautical charts, coastal survey and tidal data [Vatsa et al., 2002]. Thus, the accuracy and the adequacy of the hydrographic charts depend on the quality of the data collected during the survey [Vatsa et al., 2002]. The International Hydrographic Organization (IHO) has defined minimum standards for hydrographic surveys such as positional accuracy, sounding accuracy, sounding density in its special publication 44 (S-44). These standards are to be applied to the hydrographic charts all over the world [Van Der Wal and Pye, 2003]. The first edition of S-44 was in 1968 with its subsequent editions in 1982 and 1987. These three editions were similar as they were meant for the surveys carried out for the preparations of nautical charts which were generally used for marine navigation [Mills, 1998]. These standards require that at least 95% of the positions for the soundings in the shallow water should lie within 1.5 mm of the true positions, at the scale of the survey [Van Der Wal and Pye, 2003], i.e., for a 1:10,000 scale of survey, soundings were to be located within 15 m of their true position with a confidence of 95% probability. According to the third edition of S-44 [IHO,1987], at least 90% of the total errors in measuring depths should not exceed 30 cm for depths less than 30 m or 1% of depths for depths greater than 30 m [Mills, 1998]. Also, the distance between each sounding line should not be more than 1 cm at the scale of survey and sounding interval should not exceed 4 to 6 mm at the survey scale. NHO follows these standards and publishes the charts and other publications in total compliance with the specifications of IHO. NHO also maintains constant interaction with other

NHO and the IHO in order to ensure strict standards in products and services (<http://indiannavy.nic.in/methodology.htm>).

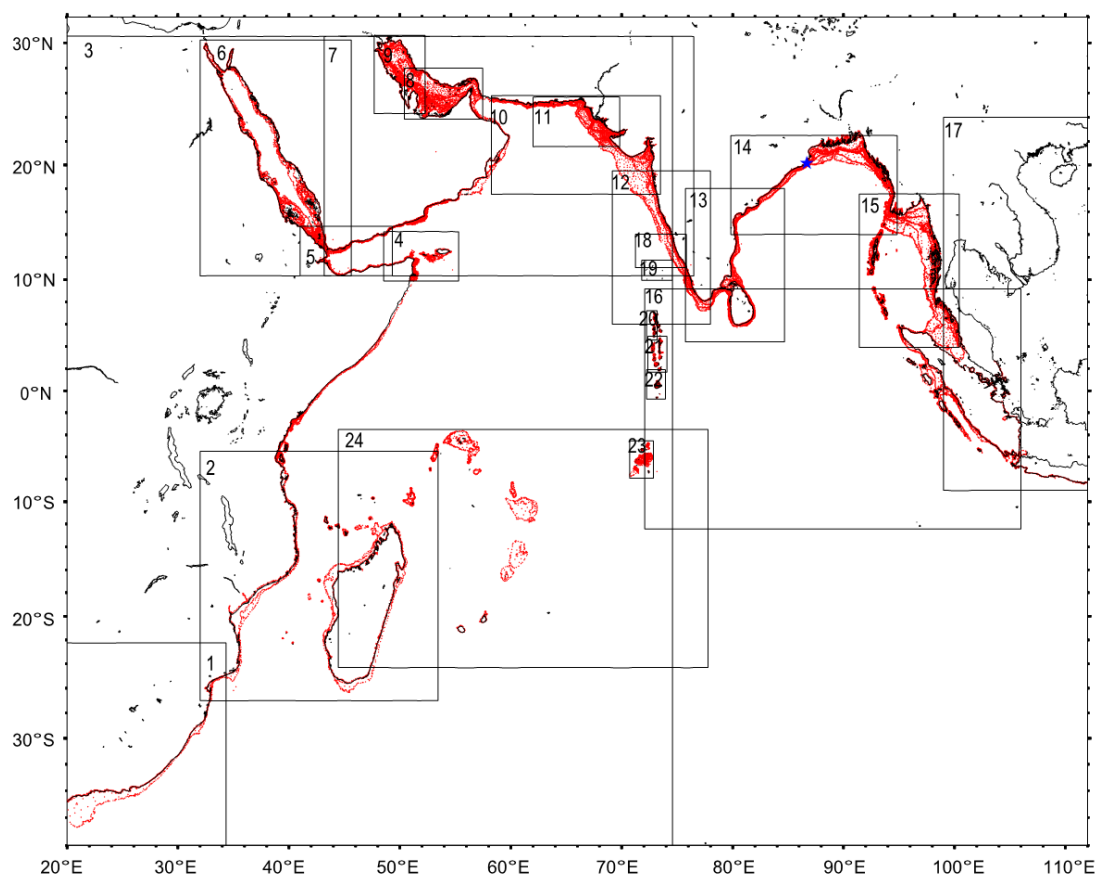
The hydrographic charts used for digitization were published during 1971-1982. Prior to the installation of automated cartographic system in NHO during 1981 [Vatsa and Kumar, 2002], the conventional hand drawn method was used to draw the contours from the lines of soundings obtained using the echo sounder trace, the soundings log and the track chart.

### **Digitization of the charts**

Digitization of the maps was carried out using the GRASS (Geographic Resources Analysis Support System) GIS (Geographic Information System) [GRASS Development Team, 2005] software. It is an open-source, free software, readily available on the web at <http://grass.itc.it>. While importing the non-georeferenced scanned maps into GRASS, they were assigned X-Y projection and the grid resolution was defined to be 1 pixel. The unreferenced map was then geo-coded by defining nine ground control points (GCPs). The accuracy of the GCPs could be checked as the software has in-built function to calculate the root mean square (RMS) error after setting at least three reference points. The RMS error is acceptable if it is less than half of the grid resolution [Neteler and Mitasova, 2002] (i.e. RMS should be less than 0.5). There is also an option to deactivate a control point if it is highly deviated from the other points. The software also allows quality control in which the geo-coded points can be checked against the actual points in the scanned maps. Thus the geo-coding was done with strict care and the RMS error obtained was less than 0.2. The results so obtained were highly accurate.

The contours digitized from the small scale charts (1:2,250,000 - 10,000,000) were 30 m and 200 m and those from the large scale charts (1:300,000 - 1,500,000) were 5, 10, 20, 30, 50, 100, 200 m. The digitization was carried out at very close intervals to capture the trends in the contours and to obtain sufficiently dense data so that the interpolation could be carried out accurately. All the sounding depths less than 200 m were also digitized.

**Figure 3.1** The boxes in the map show the regions for which the hydrographic charts were digitized. The number in each box corresponds to the number given in Table 3.1. The digitized values are also plotted.



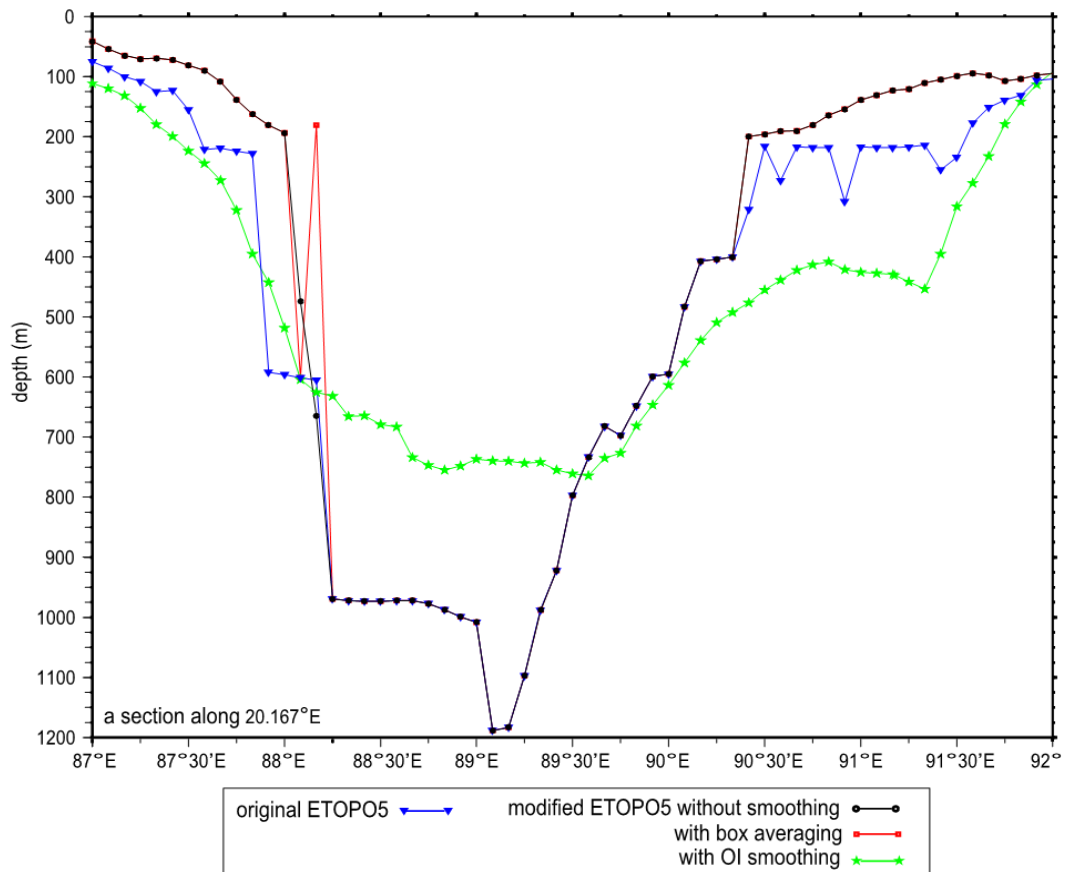
**Gridding the digitized data**

The digitized data thus obtained was averaged using a simple box averaging process called the blockmean available in the GMT (Generic Mapping Tools) [Wessel and Smith, 1998] package. The box size defined for averaging should be equal to target grid size. This averaged data was then gridded for every 5 arc minutes latitude-longitude grid using the surface program [Wessel and Smith, 1995] in the GMT package. The surface is a generalization of the minimum curvature algorithm. As mentioned earlier, DBDB5 (the major source of data for ETOPO5 dataset) is gridded using the minimum curvature spline algorithm, which is of the high-order class, and can cause undesired oscillations and false local maxima or minima [Smith and Wessel, 1990]. The "surface" program not only suppresses these effects but also prevents extrapolation by allowing the addition of a tension factor and bound constraints. The tension factor is chosen in such a way that the difference between the gridded data and the nearest digitized value is minimum in the least square sense and is fixed at 0.8. In the present work, the closed polygons with 200 m contour formed the bound constraints. We masked the values outside the polygons, so that the surface program did not produce any extrapolation. The values extrapolated on land were also masked using the options available in the GMT package.

**Blending the original and the gridded dataset**

We combined the gridded data derived with the same resolution as that of ETOPO5 with the original ETOPO5 dataset (masked for the land elevations and depths shallower than 200 m) to produce a better quality bathymetric dataset. But, the dataset obtained by simply merging the ETOPO5 with the digitized dataset showed some unrealistic features near the 200 m contour (Figure 3.2). Hence it was necessary to ensure a smooth transition between the two datasets. We experimented with a number of techniques to blend these two datasets, but none of them performed well, including the optimal interpolation method (Figure 3.2). The optimal interpolation method works best for a smoothly varying field and is dependent on the first-guess field. Since the bathymetric data have sharp gradients,

**Figure 3.2** A section of the ocean bottom topography off Paradip (20.167°N) showing comparison between different blending techniques used: simple box averaging (red) and optimal interpolation (green). Also plotted is the original ETOPO5 (blue) and modified dataset before applying smoothing (black).



especially near the continental rise where the 200 m contour generally falls, optimal interpolation was found to be inappropriate in this case. Hence, we applied a simple box averaging process to blend these datasets. In this method, the grid points that showed spurious spikes (due to merging the datasets) were picked up and then the depth value at each of these points were replaced by the average of the depth values over a box of size 10 minutes around it. The average was computed only over the ocean points and did not include the land points in the box. This method chopped off the unrealistic spikes in the dataset and kept the depths at other grid points unchanged (Figure 3.2). Thus a “modified ETOPO5” bathymetry was obtained, which is same as the original ETOPO5 in the deep ocean (greater than 200 m) but with more accurate depths derived from hydrographic charts for shallow waters (less than 200 m).

Though the region covered by the modified ETOPO5 dataset extended up to 112°E, the major concern was the improvements only in the Indian Ocean region and hence, we masked the South China Sea region in the modified datasets. Thus, the modified dataset was obtained only for the Indian Ocean region.

### **3.2.2 Models used**

Though the present thesis deals with simulations in the Bay of Bengal, we tested the improvements in the modified bathymetry by simulating the tides in the Gulf of Khambhat along the west coast of India (region indicated by dashed box in Figure 3.3) using the model developed by Unnikrishnan et al. [1999].

The model was run on 5 arc minutes spatial resolution for the same domain using the original ETOPO5 and the modified ETOPO5 bathymetric grids separately without changing any other model parameters. The accuracy of these bathymetric grids was evaluated by comparing the model results (sea surface elevation and vertically averaged current) with the tide-gauge recorded sea surface elevations at Veraval and Mumbai (Apollo Bandar) and current meter measurements in the Bombay High (19°24.5' N and 71°2.5'E) region during 24 December 1981 – 03 January 1982, which were used by Unnikrishnan et al. [1999]. The vertically averaged cross-shore (u) and alongshore (v) components of

the currents were computed from the current meter measurements available at four depths (30, 45, 60 and 75 m). These vertically averaged components included the currents generated by other processes such as winds etc., in addition to tide driven currents, whereas the currents simulated using the tidal model were driven only by tides. Thus, in order to compare the observed currents with the simulated currents, the tidal currents were to be separated from the measured currents. Hence a high pass filter with cut off at  $0.75 \text{ day}^{-1}$  was applied to the vertically averaged current in order to remove the low frequency currents.

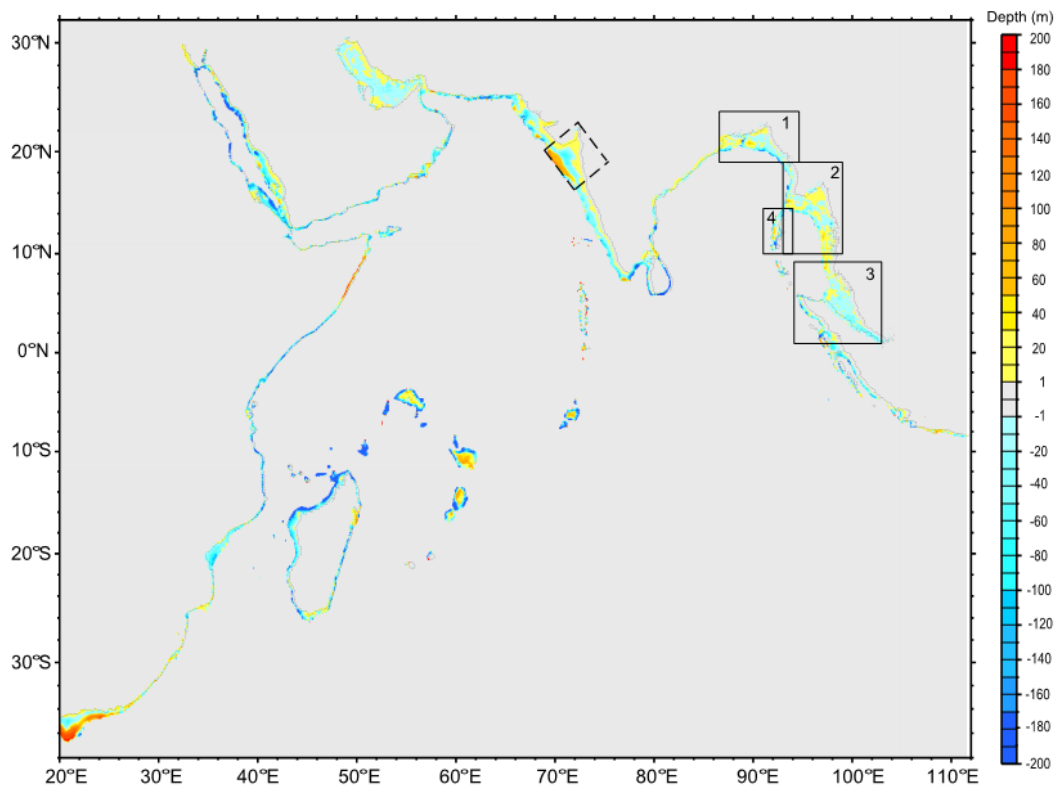
### **3.3 Results and Discussions**

#### **3.3.1 Improvements in the modified bathymetry**

There is a significant improvement in the bathymetry in many shallow regions of Indian Ocean as seen from Figure 3.3 which shows the anomaly between the modified and original ETOPO5 bathymetric datasets. The anomaly was calculated by subtracting the original data from the modified data. The lower contour levels in the original ETOPO5 results in a positive anomaly of nearly 40-60 m in the gulfs such as Gulf of Khambhat and Gulf of Martaban. High negative anomalies of about 60-80 m are found along the west coast of India and around the Madagascar Island. The ETOPO5 dataset also have a problem in representing the bathymetry near the islands and atolls as these regions show large positive anomaly in depth.

We analyzed the improvements in detail in the Bay of Bengal region which forms the domain of the numerical model used in the present study to simulate tides and storm surges. The comparison between the two datasets in other areas, such as the Red Sea, Persian Gulf, and west coast of India are illustrated in Sindhu et al. [2007]. Figures 3.4 to 3.7 show the improvements in the modified ETOPO5 dataset for the head bay, Gulf of Martaban, Malacca Strait and the Andaman islands, the regions being indicated by the boxes in Figure 3.3.

**Figure 3.3** The difference in depths (anomaly) between the modified ETOPO5 (ETOPO5 merged with the gridded digitized data) and the original ETOPO5 dataset for the Indian Ocean. The boxes mark the region shown in detail in Figures 3.4 to 3.7.





In the head bay, the original ETOPO5 dataset shows a shallow region of 40m around 90°E, 20.7°N (Figure 3.4a), thereby suggesting a sea mount like feature in the region. However, as evident from the hydrographic charts, no such feature is present in this region. The modified ETOPO5 thus yields a more realistic bathymetry for the head bay (Figure 3.4b) than the original ETOPO5 dataset. The modified bathymetry is similar to that obtained by Jakobsen et al. [2002], who derived the bathymetry for the head bay from British Admiralty Charts and BIWTA Depth Charts.

The modified ETOPO5 data set also represents the bathymetry of the Gulf of Martaban (Figure 3.5a) more accurately than the original ETOPO5 dataset (Figure 3.5b) and is similar to the bathymetry obtained by Ramaswamy et al. [2004] from a cruise of Ocean Research Vessel (ORV) Sagar Kanya.

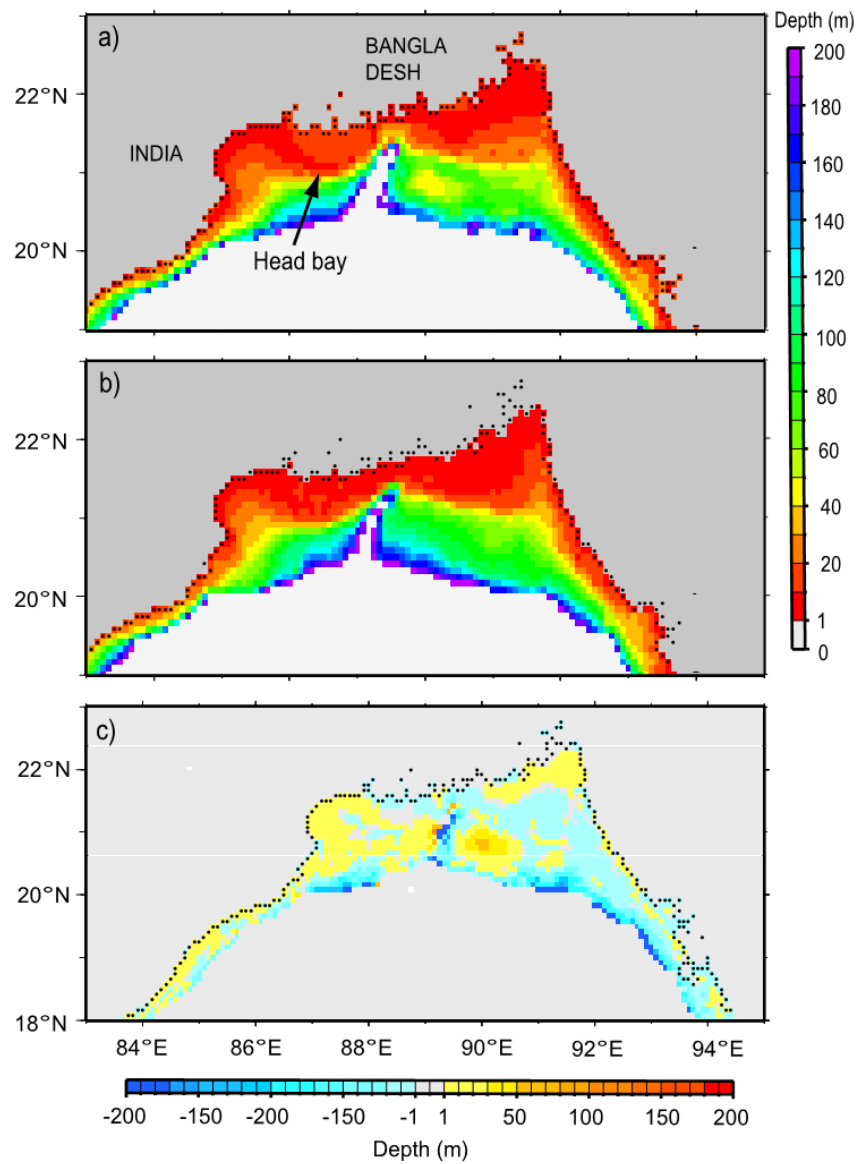
In the Malacca Strait, the modified ETOPO5 (Figure 3.6b) dataset shows shallower depths than the original dataset in south eastern end (Figure 3.6a). This is found to be consistent with hydrographic charts of the region.

The original ETOPO5 dataset shows wide shallow regions of nearly 20 m depth around the Andaman islands (Figure 3.7a), whereas the modified dataset shows depth variations up to about 60 m in this region (Figure 3.7b). The depth of the sea in the region between the Andaman and the Little Andaman Islands is greater than 200 m in the original ETOPO5 (Figure 3.7a), but in the modified bathymetry, the depths in these regions do not exceed 50 m (Figure 3.7b). This results in a negative anomaly of greater than 200 m as shown in Figure 3.7c.

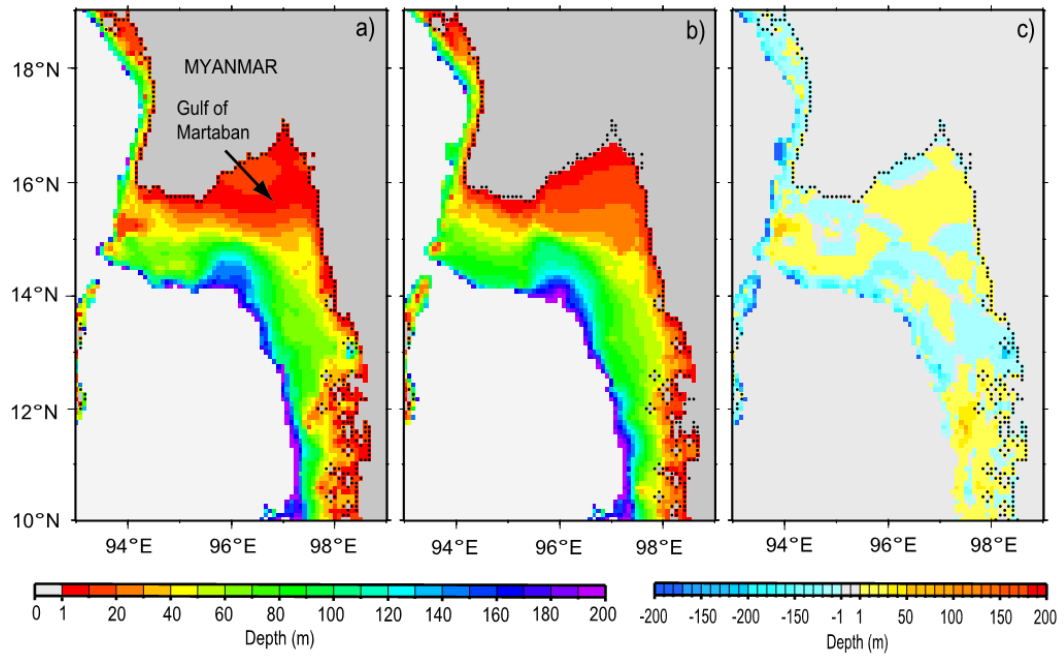
### **3.3.2 Evaluation of the modified bathymetric datasets**

We demonstrate the improvements in the modified datasets by carrying out numerical experiments with the models mentioned in Section 3.2.2 using the original and the modified ETOPO5 dataset. As mentioned earlier, the domain of this tidal model covered the Gulf of Khambhat region, in which a sea-mount like feature is observed in the original ETOPO5 dataset indicated by the positive anomaly of 40-60 m in Figure 3.3.

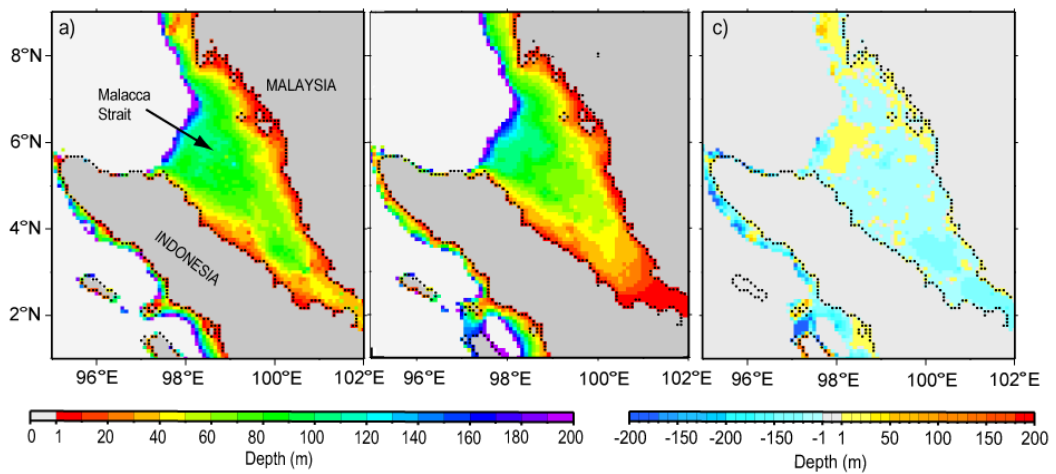
**Figure 3.4** The bathymetry obtained from the a) original ETOPO5, b) modified ETOPO5 and c) difference between them (anomaly) for the head bay.

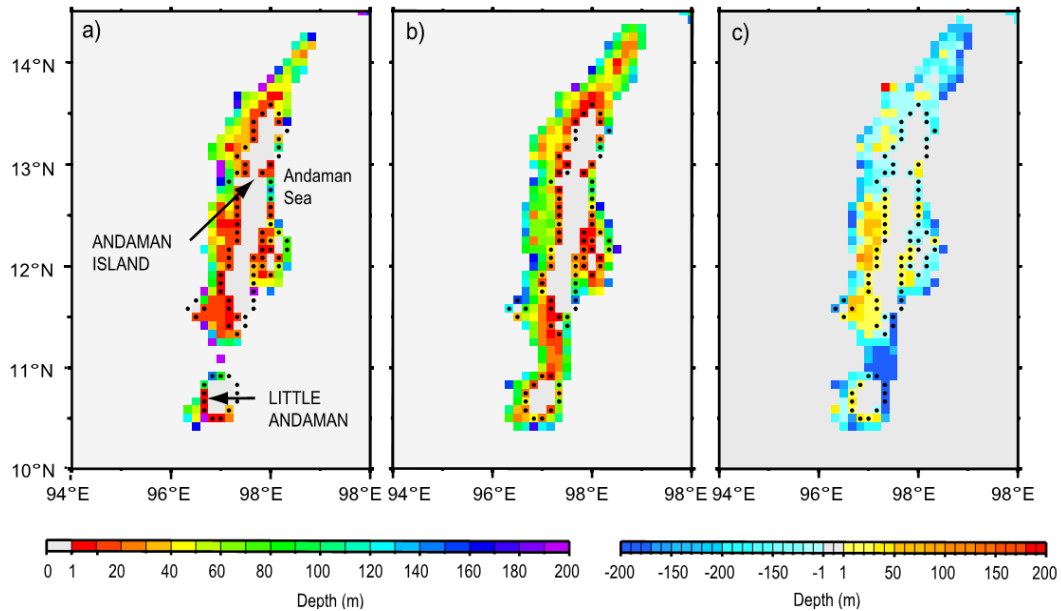


**Figure 3.5** Same as Figure 3.4, but for the Gulf of Martaban.



**Figure 3.6** Same as Figure 3.4, but for the Malacca Strait.



**Figure 3.7** Same as Figure 3.4, but for the Andaman Islands.

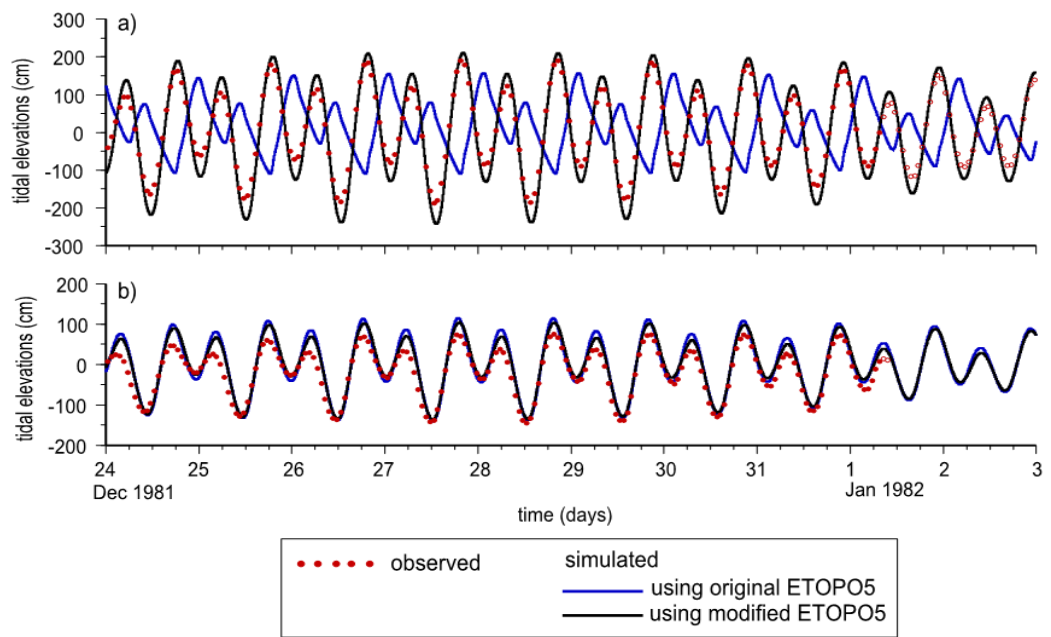
### Tidal model

Figure 3.8 provides a comparison of the simulated sea surface elevations with the observations. At Mumbai, the comparison shows a poor agreement both in amplitude and phase when the original ETOPO5 bathymetry is used, but shows a good agreement in the case of modified ETOPO5 (Figure 3.8a). At Veraval, we can see only a slight improvement in the results when the modified ETOPO5 dataset is used (Figure 3.8b). The sea-mount-like feature in the original ETOPO5 has significantly affected the simulated sea surface elevations at Mumbai.

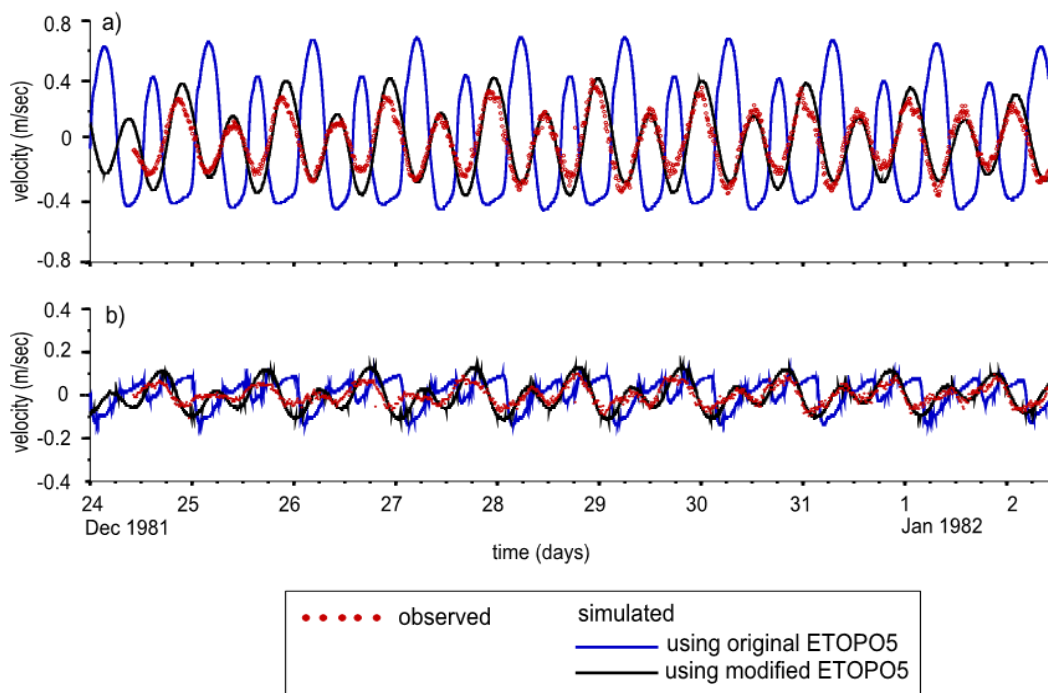
The comparison of the vertically averaged  $u$  and  $v$  components observed at Mumbai High with that obtained from the tidal model simulation (Figure 3.9a and b) clearly shows the improvement in the modified ETOPO5 bathymetric grid. The simulated  $u$  and  $v$  components obtained using the modified ETOPO5 are much closer to the observations than those obtained with the original ETOPO5.

From the discussions above, it is evident that the modified ETOPO5 dataset is an improvement over the original ETOPO5 dataset.

**Figure 3.8** The sea surface elevation observed (red dots) at a) Mumbai (Apollo Bandar) and b) Veraval and that obtained from the simulation of the tidal model when original ETOPO5 dataset (blue line) and the modified dataset (black line) are used.



**Figure 3.9** The vertically averaged a) cross-shore and b) along-shore component computed from the observed current (red dots) at Bombay High and that simulated by the tidal model during 24<sup>th</sup> December, 1981 - 3<sup>rd</sup> January, 1982 when the original (blue line) and the modified ETOPO5 (black line) is used



### **3.4 Conclusion**

We have developed an improved 5 arc bathymetric dataset derived from digitized contours and sounding depths values for the entire Indian Ocean north of 38°S and between 20°E and 112°E. The original ETOPO5 bathymetry data is shown to be inaccurate in shallow regions. In order to generate the modified dataset, the shallow depth values (less than 200 m) derived from the hydrographic charts were gridded and then blended with the deeper depth values (greater than 200m) from the original ETOPO5 dataset using appropriate merging technique to ensure smooth transition between the two dataset. We have demonstrated the improvements of the modified dataset over the original ETOPO5 dataset using a tidal circulation model. However, the drawback of the modified dataset is that the maps used for digitization are of different resolutions that lead to sparse data in some regions. The modified ETOPO5 bathymetric dataset are available at the site ([http://www.nio.org/index/option/com\\_subcategory/task/show/title/Sea-floor%20Data/tid/2/sid/18/thid/113](http://www.nio.org/index/option/com_subcategory/task/show/title/Sea-floor%20Data/tid/2/sid/18/thid/113)).